frontiers | Frontiers in Bioengineering and Biotechnology

TYPE Original Research
PUBLISHED 06 March 2025
DOI 10.3389/fbioe.2025.1537856

OPEN ACCESS

EDITED BY
Enrica Verné,
Polytechnic University of Turin, Italy

REVIEWED BY
Serhat Keser,
Firat University, Türkiye
Rakesh A. Afre,
Zeal Institute, India

*CORRESPONDENCE
Manuel Pedro Fernandes Graça,
✉ mpfg@ua.pt

RECEIVED 01 December 2024
ACCEPTED 17 February 2025
PUBLISHED 06 March 2025

CITATION
Hammami I, Fernandes Graça MP, Gavinho SR, Regadas JS, Jakka SK, Pádua AS, Silva JC, Sá-Nogueira I and Borges JP (2025) Influence of zirconium dioxide (ZrO_2) and magnetite (Fe_3O_4) additions on the structural, electrical, and biological properties of Bioglass® for metal implant coatings.
Front. Bioeng. Biotechnol. 13:1537856.
doi: 10.3389/fbioe.2025.1537856

Influence of zirconium dioxide (ZrO_2) and magnetite (Fe_3O_4) additions on the structural, electrical, and biological properties of Bioglass® for metal implant coatings

Imen Hammami[1], Manuel Pedro Fernandes Graça[1]*, Sílvia Rodrigues Gavinho[1], Joana Soares Regadas[1], Suresh Kumar Jakka[1], Ana Sofia Pádua[2], Jorge Carvalho Silva[3], Isabel Sá-Nogueira[4,5] and João Paulo Borges[2]

[1]I3N and Physics Department, Aveiro University, Aveiro, Portugal, [2]I3N-CENIMAT and Materials Science Department, NOVA School of Science and Technology, Campus de Caparica, Caparica, Portugal, [3]I3N-CENIMAT and Physics Department, NOVA School of Science and Technology, Campus de Caparica, Caparica, Portugal, [4]Associate Laboratory i4HB—Institute for Health and Bioeconomy, NOVA School of Science and Technology, NOVA University Lisbon, Caparica, Portugal, [5]UCIBIO—Applied Molecular Biosciences Unit, Department of Life Sciences, NOVA School of Science and Technology, NOVA University Lisbon, Caparica, Portugal

Background: The growing need for durable implants, driven by aging populations and increased trauma cases, highlights challenges such as limited osseointegration and biofilm formation. 45S5 Bioglass® has shown promise due to its bioactivity, antimicrobial properties, and ability to enhance osseointegration through electrical polarization. This study investigates the effects of incorporating different concentrations of ZrO_2 and Fe_3O_4 into 45S5 Bioglass® to enhance its electrical and biological properties.

Methods: Raman analysis was used to evaluate how these oxides influenced the amount of non-bridging oxygens (NBOs) and glass network connectivity. Electrical characterization was performed using impedance spectroscopy to measure conductivity and ion mobility. Antibacterial activity was assessed using the agar diffusion method, and bioactivity was evaluated through simulated body fluid (SBF) immersion tests.

Results: The results revealed that bioglasses containing ZrO_2 exhibited higher NBO content compared to Fe_3O_4, leading to improved electrical and biological properties. ZrO_2, particularly at 2 mol%, significantly enhanced conductivity, antibacterial activity, and bioactivity. In contrast, Fe_3O_4 reduced both antibacterial activity and bioactivity.

Conclusion: The findings demonstrate that ZrO_2 addition improves the electrical and biological performance of 45S5 Bioglass®, making it a promising candidate for durable implants. Fe_3O_4, however, showed limited benefits.

KEYWORDS

bioglass®, zirconium, iron, bioactivity, antibacterial activity, electrical properties, bone regeneration, implant coatings

1 Introduction

Dental implants are fundamental to contemporary restorative dentistry, providing an exceptional solution for individuals experiencing tooth loss due to aging, trauma, or disease. The global demand for dental implants has increased significantly, driven by an aging population, increased awareness of oral health, and advancements in implant technology. These implants are essential for restoring oral function, aesthetics, and overall quality of life, making them a primary focus in biomedical research (Addy, 2024; Cociuban et al., 2024). Despite significant progress, the long-term efficacy of dental implants remains uncertain. Osseointegration, the biological process through which the implant integrates with surrounding bone tissue, is crucial for stability and functionality. Titanium and its alloys, particularly Ti-6Al-4V, are widely used for their superior mechanical properties and corrosion resistance. However, they may have limitations in facilitating osseointegration (Civantos et al., 2017; Silva et al., 2022). Insufficient bone integration can lead to micromotion and gaps at the implant-bone interface, which may promote bacterial adhesion and biofilm formation. Once established, these biofilms can induce persistent infections and localized bone resorption, ultimately threatening implant success (Gbejuade et al., 2015; Davidson et al., 2019).

To address these limitations, researchers are exploring bioactive materials and coatings promoting osseointegration while reducing bacterial colonization risk. One of the most promising materials is 45S5 Bioglass® ($46.1SiO_2$-$24.4Na_2O$-$26.9CaO$-$2.6P_2O_5$ (mol%)), which gained significant attention for its ability to promote bone regeneration (Hench et al., 1971; Hench and Paschall, 1973). Initially developed in the 1970s by Larry L. Hench (Hench, 2006; Hench, 2013), these glasses possess a unique composition that allows them to bond directly to living bone tissue. Upon contact with physiological fluids, 45S5 Bioglass® undergoes a series of reactions, leading to the formation of a hydroxyapatite layer on its surface. This layer mimics the mineral component of natural bone, facilitating osseointegration. Additionally, the release of ions from the glass can inhibit bacterial growth, reducing the risk of infection (Allan et al., 2001; Allan et al., 2002; Begum et al., 2016).

The incorporation of metal ions into bioglass has emerged as a promising strategy to enhance its biological properties (Cacciotti, 2017; de Souza Balbinot et al., 2019; Malavasi et al., 2019; Aghili et al., 2022; Hammami et al., 2024). Elements such as zirconium (Zr) and iron (Fe) have garnered significant attention due to their unique characteristics. Zirconium, particularly in the form of zirconium dioxide (ZrO_2), is extensively utilized in biomedical applications due to its biocompatibility and outstanding mechanical properties, including its exceptional strength and fracture toughness, making it a widely used reinforcing agent (Silva et al., 2004; Pattnaik et al., 2011; Bhowmick et al., 2017; Kang et al., 2021). Zr can also stimulate osteoblast proliferation and differentiation, leading to accelerated bone healing (Hempel et al., 2010; Pattnaik et al., 2011; Bhowmick et al., 2017). Studies by Goo et al. (2018) and Sa et al. (2018) have demonstrated the effectiveness of ZrO_2 in promoting bone formation and improving osteogenic activity, respectively. Additionally, ZrO_2 possesses significant antimicrobial properties against various bacteria by interfering with bacterial respiration processes (Jangra et al., 2012; Fathima et al., 2017; Rad Goudarzi et al., 2019; Kumar et al., 2020).

Iron (Fe) is essential for various cellular functions, including oxygen transport and energy metabolism (Touati, 2000; Theil and Goss, 2009). Iron deficiency can lead to impaired collagen synthesis and reduced bone density (Abraham, 2014; Bose et al., 2018). Fe supports osteoblastic differentiation, proliferation, and calcification (Ullah et al., 2020; Zhu et al., 2023). Research by Long et al. (2014) and Zhou et al. (2024) has shown that incorporating Fe into biomaterials enhances cell adhesion, proliferation, and osteogenic differentiation. Fe also exhibits antibacterial properties by generating reactive oxygen species (ROS) through the Fenton reaction, which can damage bacterial cells (Touati, 2000; Behera et al., 2012; Zhang et al., 2016; Ezealigo et al., 2021).

In addition to ion insertion, electrical polarization offers a promising approach to enhance the biological properties of bioactive glass. By applying an electric field, surface charges can be induced, influencing cellular interactions and promoting tissue integration (Metwally and Stachewicz, 2019). This approach has been successfully applied to calcium-phosphate ceramics like hydroxyapatite (HA), where negative surface charges have been shown to promote bone growth and cell proliferation (Yamashita et al., 1996; Kobayashi et al., 2001; Ohgaki et al., 2001). However, the application of electrical polarization to bioglasses remains relatively unexplored. While the electrical polarization of HA is primarily driven by proton migration (Prezas et al., 2017), the higher ionic conductivity of bioglasses, mainly due to sodium ions, suggests that ion migration may play a significant role in their polarization (Obata et al., 2003; Obata et al., 2004). A deeper understanding of the electrical properties of bioglass is crucial to unlock their potential for electrical polarization, which can significantly enhance their bioactivity and overall performance in biomedical applications.

This study addresses a significant challenge in dental implantology: bacterial infections that can lead to bone loss and subsequent implant failure. To mitigate this issue, we developed a material for implant coating based on 45S5 bioglass®, incorporating varying concentrations of zirconium dioxide (ZrO_2) and magnetite (Fe_3O_4). The melt-quenching technique used in this study offers significant advantages in terms of scaling up the production of these materials for clinical use. This method allows for the fabrication of bioactive glasses in large quantities at a relatively low cost compared to other techniques, such as sol-gel. Its reliability and efficiency make it a promising approach for large-scale production, which is essential for practical applications in clinical settings. The influence of these

TABLE 1 Composition of different bioglass samples.

Composition (mol%)						
Sample	SiO_2	Na_2O	CaO	P_2O_5	ZrO_2	Fe_3O_4
BG	46.10	24.40	26.90	2.60	-	-
Zr1	45.64	24.16	26.63	2.57	1	-
Zr2	45.18	23.91	26.36	2.55	2	-
Zr4	44.26	23.42	25.82	2.50	4	-
Fe1	45.64	24.16	26.63	2.57	-	1
Fe2	45.18	23.91	26.36	2.55	-	2
Fe4	44.26	23.42	25.82	2.50	-	4

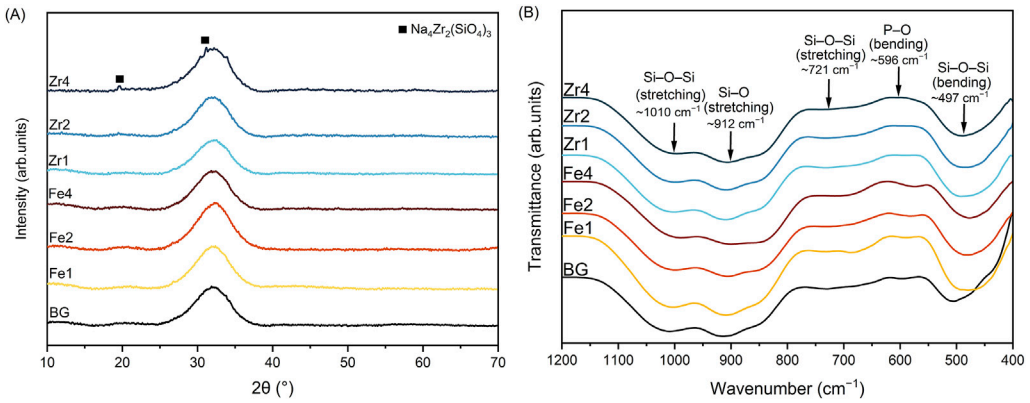

FIGURE 1
(A) XRD patterns, and **(B)** FTIR spectra of the bioglass samples.

metal oxides on the structural properties of 45S5 bioglass was examined using X-ray diffraction (XRD), Fourier-transform infrared (FTIR), and Raman spectroscopy. Given bioglass's potential for electrical charge storage, impedance spectroscopy (IS) was employed to investigate its electrical properties and the impact of oxide additions. To evaluate the potential of the prepared glasses as implant coating materials, a cytotoxicity assay was conducted using the extract method and human osteosarcoma (Saos-2) cells. The antibacterial activity of the different bioglass compositions was assessed using the agar diffusion method against *Escherichia coli*, *Staphylococcus aureus*, and *Streptococcus mutans*. The bioactivity assay was assessed by immersing the samples in a Simulated Body Fluid (SBF) solution.

2 Materials and methods

2.1 Bioglass synthesis

Bioglass samples were fabricated using the melt-quenching technique, adhering to the 45S5 Bioglass® composition (46.1SiO_2-24.4Na_2O-26.9CaO-2.6P_2O_5 (mol%)) as described by Hench et al. (1971), Hench and Paschall (1973). Various concentrations (1, 2, and 4 mol%) of ZO_2 (Zr1, Zr2, Zr4) and Fe_3O_4 (Fe1, Fe2, Fe4) were incorporated into the bioglass network. High-purity (≥99%) chemical precursors (SiO_2, P_2O_5, $CaCO_3$, Na_2CO_3, and $(ZrO(NO_3)_2•XH_2O$; X~3) or Fe_3O_4), supplied by sigma-Aldrich, were mixed using a planetary ball mill system for 1 h at 300 rpm. The resulting mixture was calcined at 800 °C for 8 h, followed by melting at 1,400 °C for 1 h. To enhance homogeneity, the melt was re-melted under identical conditions. The resulting bulk glass was ground and milled using planetary ball milling process, to obtain the final bioglass powders. These synthesis parameters were consistently applied to all the compositions, including the varying concentrations of ZrO_2 (1, 2, and 4 mol%) and Fe_3O_4 (1, 2, and 4 mol%). The selected parameters were verified to ensure reproducibility, with the combination of visual inspection and re-melting steps confirming the suitability of the process for producing homogeneous bioglass samples. The nominal compositions of the prepared bioglass samples are presented in Table 1.

2.2 Structural characterization

X-ray diffraction (XRD) analysis was performed using a Panalytical Aeris diffractometer with Cu Kα radiation (λ =

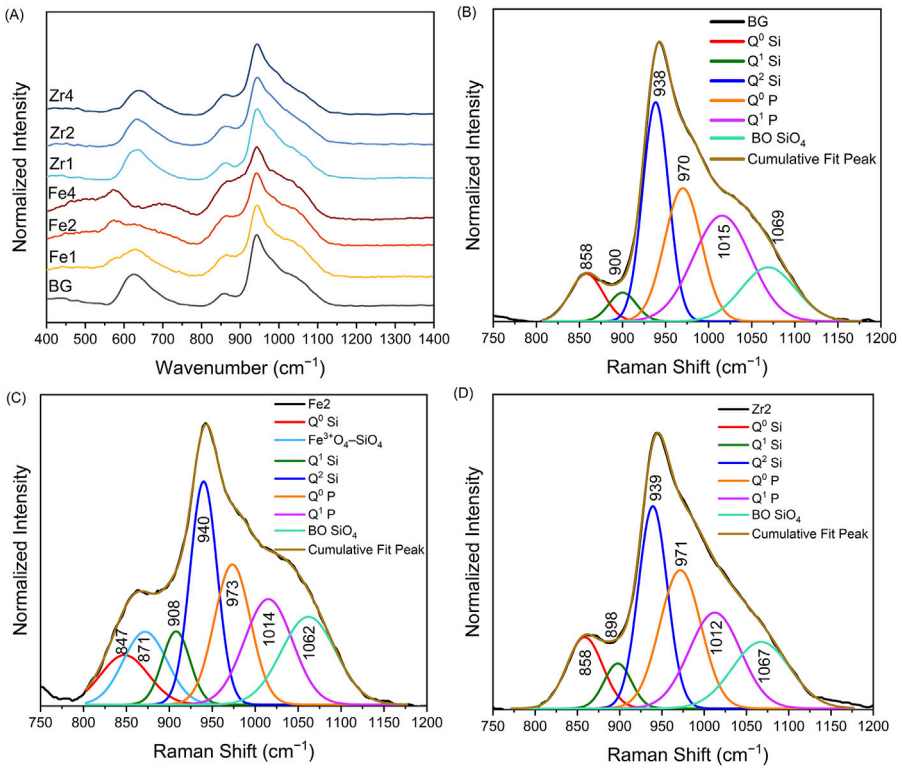

FIGURE 2
(A) Raman spectra of different bioglasses; deconvoluted Raman spectra of **(B)** BG, **(C)** Fe2, and **(D)** Zr2 bioglasses.

1.54056 Å). Data were collected over a 2θ range of 10°–70° with a step size of 0.002°.

Fourier Transform Infrared (FTIR) spectroscopic analysis was performed using a PerkinElmer Spectrum BX spectrometer equipped with a Golden Gate Diamond Attenuated Total Reflectance (ATR) accessory. Powdered samples were analysed at room temperature and humidity (approximately 23°C and 35%) over a spectral range of 400–1,200 cm^{-1}.

Raman spectroscopic analysis was conducted on the bulk samples using a Jobin Yvon HR800 spectrometer. An Ar^+ laser (λ = 532 nm) was employed, and spectra were acquired in backscattering geometry over the spectral range of 200–1,400 cm^{-1}.

2.3 Electrical properties

Electrical measurements were performed on 1 mm-thick bulk glass samples. Silver conducting paste was applied to the opposing parallel surfaces of the samples to establish good electrical contact. Both direct current (DC) and alternating current (AC) measurements were conducted in a nitrogen bath cryostat, enabling precise temperature control within a range of 100–400 K. An Oxford Research IT-C4 system equipped with a platinum sensor was used to monitor and control the sample temperature. DC conductivity measurements were performed using a Keithley 617A electrometer, applying a constant voltage of 100 V across the bulk glass sample. AC impedance spectroscopy measurements were carried out using an Agilent 4294A impedance analyser over a frequency range of 100 Hz to 1 MHz, employing the C_p–R_p configuration and applying an ac signal of 0.5 V. The complex permittivity (ε*) and complex modulus (M*) were calculated using the following Equations (Graça et al., 2012; Ashok et al., 2017; Barsoukov and Macdonald, 2018).

$$\varepsilon^* = \varepsilon' - j\varepsilon'' = C_p \frac{d}{\varepsilon_0 A} - i\,d\,(\omega R_P \varepsilon_0 A)$$

$$M^* = \frac{1}{\varepsilon^*} = M' + iM'' = \frac{\varepsilon'}{\varepsilon'^2 + \varepsilon''^2} + i\frac{\varepsilon''}{\varepsilon'^2 + \varepsilon''^2}$$

where C_p and R_p are the measured capacitance and resistance, d is the sample thickness, A is the electrode area, ω is the angular frequency, and ε_0 is the permittivity of the free space (8.8542 × 10^{-12} F/m).

The complex ac conductivity (σ_{ac}) was calculated using the following relation (El-Mallawany, 2014; Barsoukov and Macdonald, 2018):

$$\sigma_{ac}{}^* = \varepsilon_0 \omega \varepsilon'' + i\varepsilon_0 \omega \varepsilon'$$

The activation energy (Ea) for both AC and DC conductivity was determined by fitting the temperature-dependent conductivity data to the Arrhenius equation (Macdonald, 1987; Barsoukov and Macdonald, 2018).

$$\sigma = \sigma_0 \exp\left(\frac{-E_a}{k_B T}\right)$$

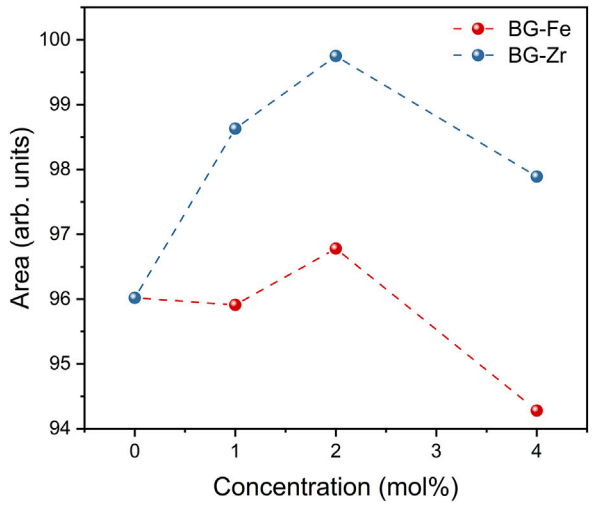

FIGURE 3
The sum of the areas of the Raman vibration bands associated with NBOs.

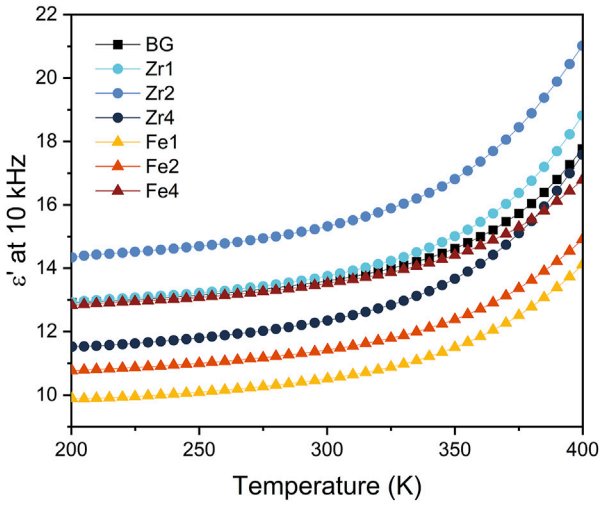

FIGURE 4
The variation dielectric constant, ε', as a function of the temperature for all bioglass samples.

where σ_0 is a pre-exponential factor, E_A is the activation energy, K_B is the Boltzmann constant, and T is the temperature.

2.4 Cytotoxicity assay

The cytotoxicity of the bioglass powders was evaluated using a standard extract test with human osteosarcoma (Saos-2) cells (ATCC® HTB-85™), following the International Standard ISO 10993-5. Samples were sterilized at 120 °C for 2 h prior to testing. Non-passivated extracts were prepared by incubating the powders in McCoy 5A medium at a concentration of 100 mg/mL for 24 h at 37°C, followed by filtration. For the passivated extract, the filtered powders were re-incubated in fresh McCoy 5A medium for 24 h. Saos-2 cells were seeded in 96-well plates at a density of 30,000 cells/cm^2, incubated for 24 h at 37°C in a 5% CO_2 atmosphere, and then exposed to the diluted extracts (50%, 25%, 12.5%, and 6.25%). A positive control, consisting of cells exposed to a cytotoxic environment induced by 10% dimethyl sulfoxide (DMSO), and a negative control of viable cells were included. After 48 h, Cytotoxicity was evaluated after 48 h of cell incubation with the extracts and their dilutions using a resazurin-based colorimetric assay. Cell viability was assessed by measuring the absorbance of each well at 570 nm and 600 nm using a BioTek ELx800UV microplate reader. Each experiment was performed in triplicate, each comprising six technical replicates.

2.5 Antibacterial activity

The antibacterial properties of the bioglass compositions were assessed using an agar diffusion assay. Reference strains of *E.scherichia coli* K12, *Staphylococcus aureus* COL MRSA (methicillin-resistant), and *Streptococcus mutans* DSM20523 were cultured overnight in tryptic soy broth (TSB) at 37°C. Tryptic Soy Broth (TSB) medium solidified with Tryptic Soy Agar (TSA) was used to prepare two-layer bioassay plates. The base layer was 1.5% w/v and the top layer was 0.8% w/v. The top layer was inoculated with approximately 10^8 CFU/mL of the appropriate indicator bacteria. Sterilized cylindrical bioglass pellets (6 mm diameter, ~2 mm thick) were placed on agar plates, and incubated for 24 h at 37°C. *S. mutans* plates were incubated in a 5% CO_2 atmosphere. Zones of inhibition were measured to determine the antibacterial efficacy of the bioglass compositions. To analyse the statistical significance of the results, an unpaired t-test was performed on the data from eight independent assays for each bacterial strain. Statistical comparisons between the base bioglass composition and the modified compositions were conducted using GraphPad Prism 8.0 software.

2.6 Bioactivity assay

Bioactivity assessments were performed following the International standard ISO 23317:2017. Bioactive glass pellets with 7 mm in diameter were immersed in simulated body fluid (SBF) and incubated at 37°C with orbital shaking for 12, 24, 48, 96 h, 14, and 28 d. SBF solution was refreshed every 48 h to simulate physiological conditions. The SBF volume (V_S) for each pellet was calculated using:

$$V_s = 100\,mm \times S_a$$

Where V_S represents the SBF volume in mm^3, and S_A denotes the pellet's surface area in mm^2.

Following incubation, the pellets were extracted from the SBF, gently rinsed with deionized water, and subsequently dried at room temperature. The morphological and compositional alterations induced by the reaction with SBF were examined using scanning electron microscopy-energy dispersive X-ray spectroscopy (SEM-EDS).

TABLE 2 The dielectric constant (ε′), dielectric loss (tan δ), AC, conductivity (σ_{AC}), AC, activation energy E_a (AC), DC conductivity (σ_{DC}), and DC activation energy E_a (DC) for all BG samples.

Sample	ε′	tan δ (10^{-2})	σ_{ac} (10^{-7}) [S/m]	E_a (AC) [kJ/mol]	σ_{dc} (10^{-9}) [S/m]	E_a (DC) [kJ/mol]
	(300 K; 10 kHz)			(10 kHz)	(300 K)	
BG	13.59 ± 0.72	1.58 ± 0.02	1.19 ± 0.01	37.95 ± 0.98	0.91 ± 0.08	75.82 ± 0.79
Zr1	13.75 ± 1.92	2.02 ± 0.01	1.54 ± 0.07	39.09 ± 0.92	1.61 ± 0.16	73.20 ± 0.76
Zr2	15.32 ± 1.95	2.28 ± 0.03	1.94 ± 0.04	37.90 ± 0.78	1.19 ± 0.17	75.96 ± 0.79
Zr4	12.34 ± 1.53	2.37 ± 0.01	1.62 ± 0.09	38.68 ± 0.87	1.45 ± 0.19	73.20 ± 0.76
Fe1	10.51 ± 1.02	1.93 ± 0.03	1.13 ± 0.02	36.97 ± 0.64	0.25 ± 0.04	80.52 ± 0.62
Fe2	11.42 ± 1.68	1.7 ± 0.02	1.14 ± 0.06	36.55 ± 0.69	0.71 ± 0.07	75.65 ± 0.44
Fe4	13.52 ± 1.23	1.45 ± 0.02	1.09 ± 0.03	35.20 ± 0.75	0.09 ± 0.002	85.94 ± 0.89

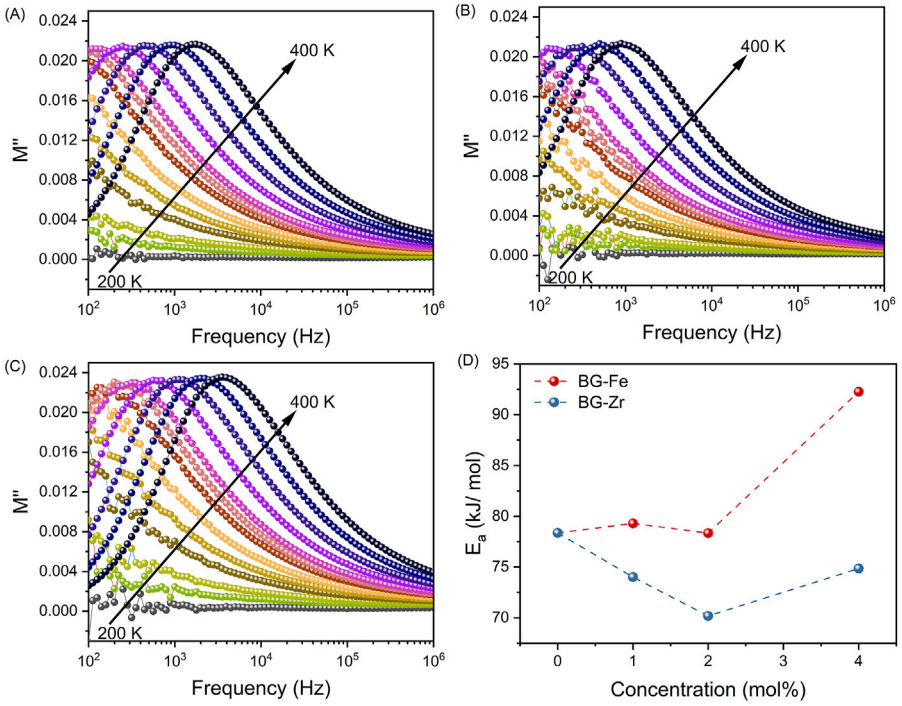

FIGURE 5
The imaginary part of the electrical modulus M″ versus frequency for **(A)** BG, **(B)** Fe4, and **(C)** Zr4 samples; **(D)** The variation of the activation energy E_a with increasing ZrO_2 and Fe_3O_4 concentration.

3 Results and discussion

3.1 Structural characterization

Figure 1A presents XRD patterns of all synthesized bioglass samples. The 45S5 Bioglass (referred to as BG) displayed a broad diffraction peak between 25° and 38°, characteristic of amorphous materials. This indicates the absence of long-range atomic order within the glass structure (Lopes et al., 2014; Araujo et al., 2020). The addition of Fe_3O_4 did not alter the bioglass structure. Similarly, a small content of ZrO_2 (2 mol%) maintained the glass's amorphous nature. However, increasing ZrO_2 concentration led to the emergence of a crystalline phase identified as sodium zirconium silicate ($Na_4Zr_2(SiO_4)_3$) with a hexagonal crystal structure.

Figure 1B depicts the FTIR spectra of the prepared bioglass samples. The BG exhibits prominent absorption bands at approximately 1,010, 912, 721, 596, and 497 cm^{-1}. The bands at 1,010 cm^{-1} and 721 cm^{-1} correspond to Si-O-Si stretching vibrations (Boccaccini et al., 2007; Ibrahim et al., 2017; Ibrahim et al., 2018). The presence of a band at 912 cm^{-1} indicates the existence of non-bridging oxygen ions (NBOs), associated with Si-O-NBO stretching (Boccaccini et al., 2007; Ibrahim et al., 2017; Ibrahim et al., 2018). The band at 596 cm^{-1} is attributed to P-O bending vibrations in amorphous phosphate, while the band at 497 cm^{-1} corresponds to

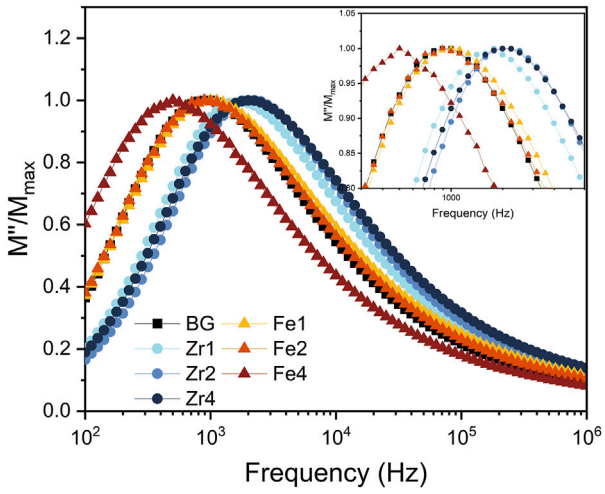

FIGURE 6
The normalized imaginary part of the modulus M''/M''_{max} versus the frequency at 390 K for all bioglasses.

Si-O-Si bending vibrations (Boccaccini et al., 2007; Dziadek et al., 2016; El-Rashidy et al., 2017; Ibrahim et al., 2017; Ibrahim et al., 2018). The incorporation of Fe_3O_4 and ZrO_2 does not significantly alter the FTIR spectra of the bioglass.

The Raman spectra of all bioglass compositions are shown in Figure 2A. The BG spectrum can be divided into two regions: low-wavenumber (<750 cm^{-1}) and high-wavenumber (>750 cm^{-1}). The broad band at 630 cm^{-1} in the low-wavenumber region is attributed to the rocking motion of bridging oxygen (BO) in structural units containing non-bridging oxygen (NBO) and symmetric Si-O-Si bending of three-membered rings (Aguiar et al., 2008; Aguiar et al., 2009; Lopes et al., 2014). In the high-wavenumber region, the deconvoluted Raman spectrum (Figure 2B) reveals six vibrational modes at approximately 858, 900, 938, 970, 1,015, and 1,069 cm^{-1}. These modes correspond to the symmetric stretching of Q^0 Si, Q^1 Si, Q^2 Si, Q^0 P, Q^1 P units, and BO in all Q Si species, respectively (Aguiar et al., 2009; Dziadek et al., 2016; Araujo et al., 2020). The addition of Fe_3O_4 modifies the glass structure, as evidenced by the Raman spectra in Figure 2C. As the Fe_3O_4 content rises, the intensity of the band at 630 cm^{-1} decreases, and new bands emerge. The appearance of a band at approximately 730 cm^{-1} is associated with the formation of Fe-related structural units, as reported in the literature for nano-Fe_3O_4 and Fe_3O_4-doped silicate glasses (Li et al., 2012; Nayak and Desa, 2018). Additionally, the emergence of bands at 560 cm^{-1} and 480 cm^{-1}, which intensify with increasing Fe_3O_4 content, correlates with the vibrational modes of hematite (Chamritski and Burns, 2005; Zhang et al., 2022). In the high-wavenumber region, the deconvolution of the Raman spectra in Figure 4. 8 reveals a new band around 880 cm^{-1} for Fe_3O_4-modified glasses, with its intensity increasing with Fe_3O_4 content. This band is associated with vibrations involving Fe^{3+}-O-Si bridging oxygen atoms or a coupled $Fe^{3+}O_4$-SiO_4 mode (Wang et al., 1995; Di Muro et al., 2009; Baert et al., 2011). The formation of these new bonds suggests increased rigidity within the glass network. The addition of ZrO_2 does not substantially modify the Raman spectra of the bioglass. Figure 2D illustrates the deconvoluted Raman spectra for the Zr2 samples, emphasizing the changes in the intensity of vibrational bands associated with NBOs.

Figure 3 shows the sum of the area of Raman vibration bands associated with NBOs (Q^0, Q^1, Q^2, and Q^3 units) for the bioglasses modified with ZrO_2 and Fe_3O_4. The incorporation of up to 2 mol% ZrO_2 leads to an increase in NBO concentration. Conversely, further ZrO_2 addition to 4 mol% results in a decline in NBOs, likely due to the formation of crystalline phases, as evidenced by XRD data, which increases the glass network's connectivity. For bioglasses modified with Fe_3O_4, a slight NBO increase was observed in the glass with 2mol% Fe_3O_4 compared to the 45S5 bioglass, followed by a decrease with higher Fe_3O_4 content. This can be attributed to the emergence of the coupled $Fe^{3+}O_4$–SiO_4 mode, (Figure 2C), suggesting that Fe forms new bonds with silica tetrahedra, thereby increasing the glass network's rigidity.

3.2 Electrical properties

Figure 4 shows the variation of the dielectric permittivity (ε') with temperature at a fixed frequency of 10 kHz. The dielectric

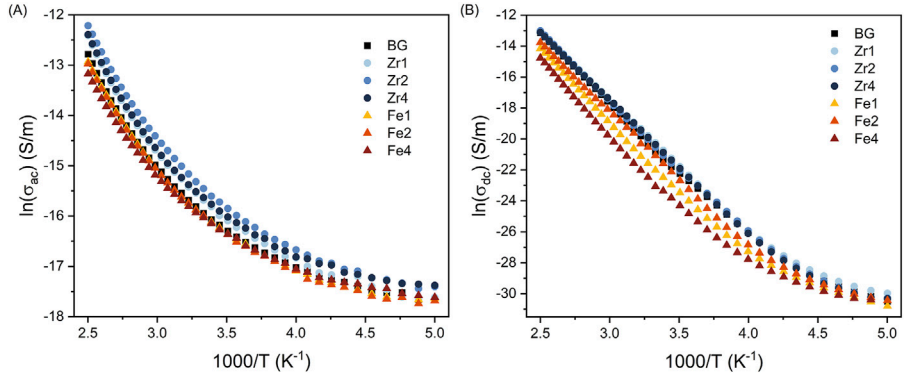

FIGURE 7
(A) AC conductivity at 10 kHz and **(B)** DC conductivity versus 1,000/T for the bioglass samples.

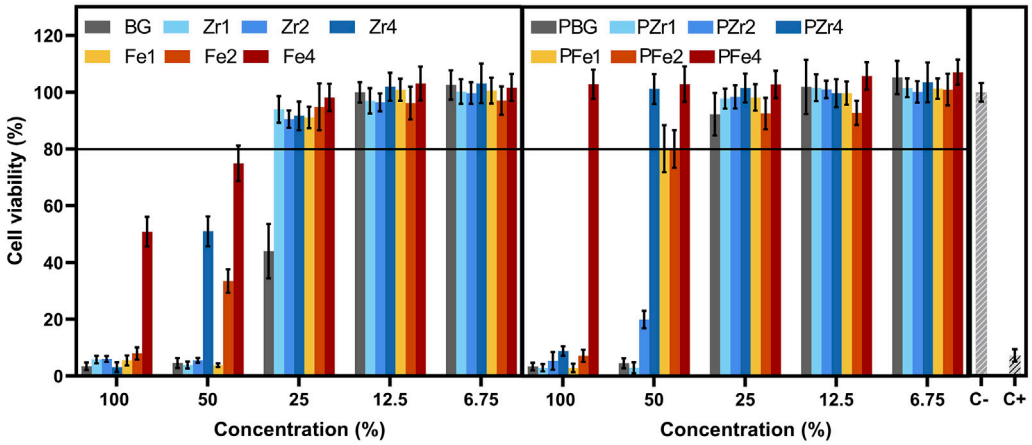

FIGURE 8
Cell viability of osteosarcoma cell line (Saos-2) after incubation with non-passivated (on the right) and passivated (on the left) bioglass extracts.

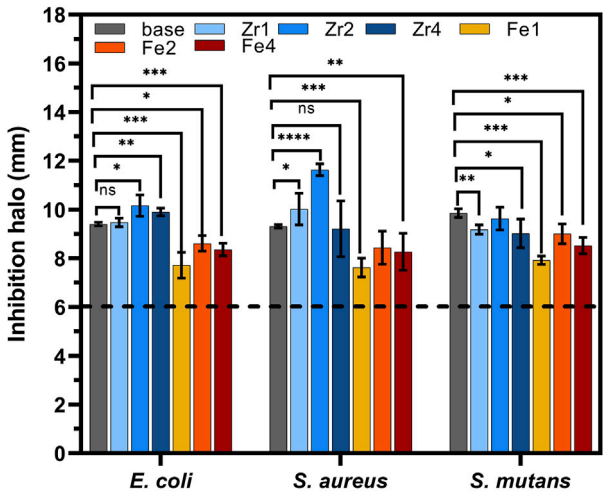

FIGURE 9
Measurement of the inhibition halo diameters of all samples against *E. coli*, *S. aureus*, and *S. mutans* bacteria after incubation for 24 h (statistical analysis was performed using unpaired t-test and the *p*-values indicate the statistical significance; ns: non-significant; $*p \leq 0.05$; $**p \leq 0.01$; $***p \leq 0.001$; $****p \leq 0.0001$).

constant increases with rising temperature in all samples which can be ascribed to the increased mobility of dipoles within the glass network at higher temperatures. This thermally activated dipole reorientation enhances the material's polarizability under the applied electric field, leading to higher dielectric constant values. Based on Figure 4 and Table 2, the insertion of ZrO_2 and Fe_3O_4 into the glasses network affects the dielectric constant values. A decrease in dielectric constant was observed for all glasses modified with Fe_3O_4 compared to the 45S5 bioglass. Furthermore, an increase in the dielectric constant was noted as the Fe_3O_4 concentration in the bioglass network increased. This increase can be attributed to the structural modifications introduced by the Fe_3O_4 addition. Raman spectroscopy revealed the formation of Fe^{3+}-O-Si bonds and Fe-related structural units. These bonds enhance the polarizability of the glass network due to the high ionic polarizability of Fe^{3+} ions and the localized dipoles formed within the structure. Furthermore, the incorporation of 4 mol% Fe_3O_4 reduces the concentration of non-bridging oxygen ions (NBOs), leading to increased network connectivity (Figure 3). Although the glass rigidity at high Fe_3O_4 content, the greater polarizability introduced by Fe-related units dominates, resulting in an overall enhancement of the dielectric constant. In contrast, the ZrO_2-modified glasses exhibit a different trend. While initial additions of ZrO_2 (up to 2 mol%) lead to a slight increase in the dielectric constant due to increased NBOs, further increases in the concentration of ZrO_2 to 4 mol% result in a decrease in the dielectric constant. This decrease could be related to the presence of the $Na_4Zr_2(SiO_4)_3$ crystalline phase, which increases the rigidity of the bioglass, leading to a reduction in NBOs and, consequently, a lower dielectric constant.

The dielectric properties of the bioglasses were investigated using the modulus formalism (M*). This approach mitigates the influence of low-frequency effects, such as electrode polarization and conductivity, providing a clearer view of the dielectric relaxation processes (Silva et al., 2005). As shown in Figure 5, a single relaxation peak is observed, which shifts to higher frequencies with increasing temperature, indicating a thermally activated mechanism. This relaxation behaviour, more evident in the modulus representation than in other representations like permittivity or impedance, is attributed to the formation of dipoles involving network modifier ions and NBOs. The activation energy (E_a) associated with the dielectric relaxation process was determined from the temperature dependence of the relaxation frequency, obtained from the imaginary part of the electrical modulus (M″), and analysing the data with the Arrhenius model (Figure 5D). Adding a low concentration of ZrO_2 (up to 2 mol%) to the bioglass network decreases the activation energy. This can be attributed to the network-modifying role of ZrO_2, which breaks down the silica network and introduces NBO sites. This increased disorder facilitates ion movement, lowering the activation energy. As ZrO_2 concentration rises, its role shifts towards network stabilization, leading to a decrease in NBOs and increased structural integrity. The

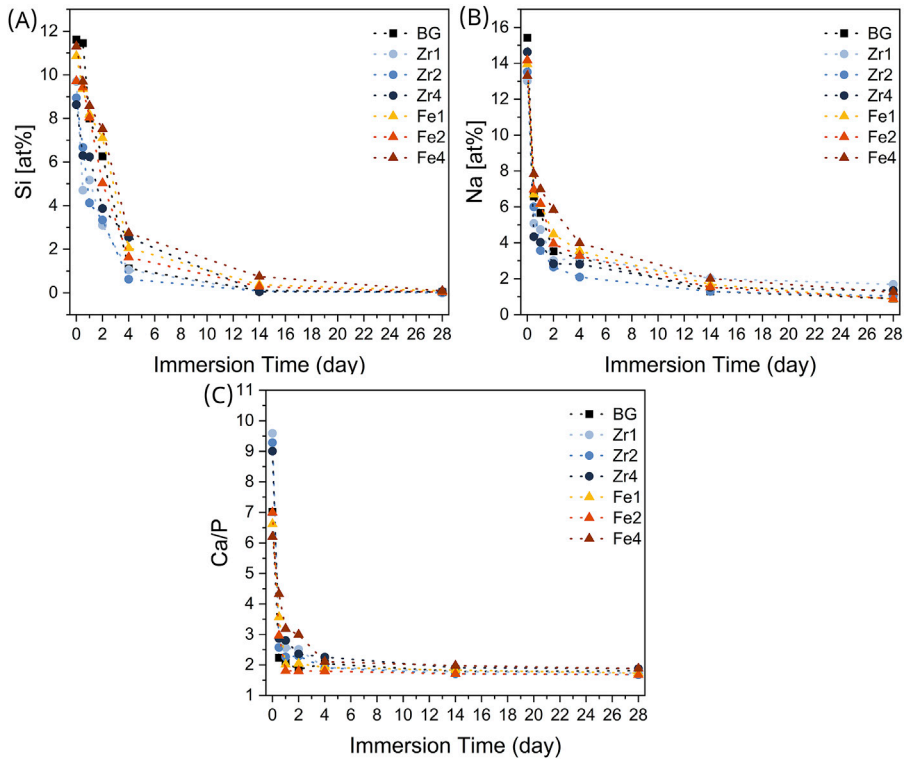

FIGURE 10
Variation of the atomic percentage of **(A)** silicon, **(B)** sodium ions, and **(C)** the ratio between calcium and phosphorous, presented on the surface of the bioglasses after SBF immersion.

emergence of crystalline phases, as observed in the XRD patterns, further supports this network polymerization. Consequently, the activation energy increases as ions and dipoles require more energy to relax within the more rigid network. Regarding the effect of Fe_3O_4, the addition of low concentrations (up to 2 mol%) does not significantly affect the activation energy. However, at higher Fe_3O_4 concentrations, the activation energy increases, suggesting increased network rigidity. This is attributed to the formation of new cross-linking bonds between Fe ions and silica tetrahedra, as evidenced by Raman spectroscopy. The increased network connectivity and reduced NBOs hinder ion mobility, leading to higher activation energies. Moreover, it is noted that the activation energy for Fe_3O_4-modified bioglasses is higher than that of ZrO_2-modified bioglasses due to the stronger cross-linking effect of Fe^{3+}-O-Si bonds. The weaker connectivity in bioglasses with ZrO_2 compared to those with Fe_3O_4, as evidenced in Figure 3 by the higher NBOs in ZrO_2-modified bioglasses, results in lower E_a. This highlights the greater impact of Fe_3O_4 on network reinforcement.

Figure 6 depicts the normalized imaginary part of the electric modulus (M''/M''_{max}) versus frequency for all bioglass samples. It can be seen that the insertion of ZrO_2 into the glass network shifts the relaxation peak to higher frequencies, corresponding to a decrease in relaxation time. In contrast, the addition of Fe_3O_4 up to 2 mol% does not significantly affect the relaxation behaviour. However, further increasing the Fe_3O_4 content to 4 mol% shifts the relaxation peak to lower frequencies, suggesting an increase in relaxation time. This suggests that excess Fe_3O_4 restricts the alignment of dipoles within the glass network in response to an applied electric field. The observed variations in relaxation behaviour are attributed to structural modifications within the glass, specifically related to alterations in the NBOs content.

Figures 7A, B illustrate the temperature dependence of AC and DC conductivity on a logarithmic scale, respectively. As expected, conductivity increases with temperature due to enhanced charge carrier mobility. Above 270 K, the conductivity exhibits a linear relationship with temperature, enabling the determination of activation energy using the Arrhenius equation. Within this temperature range, ionic conductivity surpasses electronic conductivity, making ion transport the dominant conduction mechanism in these glasses. The conductivity of the bioglass is mainly attributed to the movement of network modifiers ions (such as Na^+ and Ca^{2+}) through the glass network (Obata et al., 2003; Keshri et al., 2021; Gavinho et al., 2024).

Table 2 reveals that the activation energy for DC conductivity exceeds that of AC conductivity. This disparity can be explained by the distinct nature of ion movement in each conduction type. DC conductivity necessitates long-range charge migration, whereas AC conductivity involves shorter, localized ion displacements. Therefore, DC conduction encounters higher energy barriers, resulting in a higher activation energy requirement (Kawamura et al., 2007; Hammami et al., 2022). Additionally, as shown in Table 2 and Figure 7, the incorporation of ZrO_2 into the bioglass enhances both AC and DC conductivity, while the addition of Fe_3O_4 results in a decrease in both AC and DC conductivity. This can be

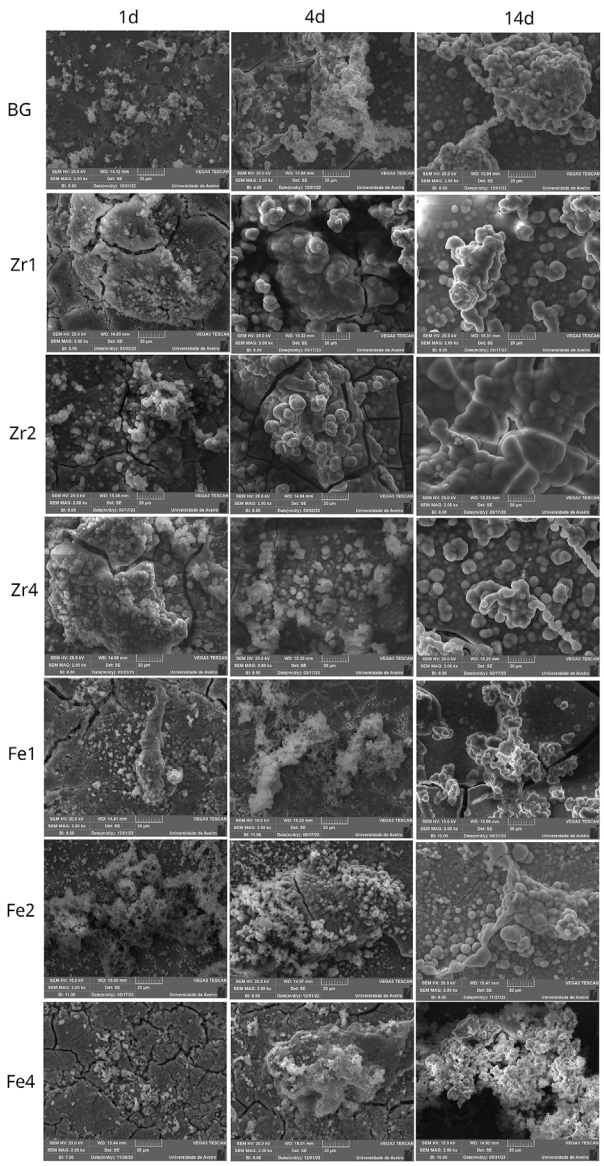

FIGURE 11
SEM micrographs of different bioglass surfaces after immersion in SBF for 1 d, 4 d, and 14 d.

attributed to the fact that ZrO_2 insertion reduces the glass network's rigidity, increasing the number of NBOs and consequently enhancing the mobility of modifier ions such as Na^+ and Ca^{2+}. Conversely, the addition of Fe_3O_4, especially at high concentrations, strengthens the glass structure by forming new cross-linking bonds with silica tetrahedra and therefore reducing ions mobility.

Overall, the structural transformations and changes in network connectivity (observed by XRD and Raman analysis) induced by oxide insertions played a crucial role in the observed electrical properties by influencing the mobility of network modifier ions (Na^+ and Ca^{2+}). In depolymerized glass networks with higher NBO content, these ions exhibit enhanced mobility, which improves the glass's electrical properties. The bioglass modified with 2 mol% ZrO_2, which exhibited a less rigid structure due to increased NBOs content (Figure 3), showed the highest dielectric constant and conductivity (Table 2). In contrast, at 4 mol% ZrO_2, the formation of crystalline $Na_4Zr_2(SiO_4)_3$ phase (Figure 1A) reduced the number of NBO, increasing the network rigidity, and consequently decreasing these properties. For Fe_3O_4-modified bioglasses, higher Fe_3O_4 concentrations increased the dielectric constant due to the formation of Fe^{3+}-O-Si bonds and Fe-related units (as shown by Raman analysis - Figure 2), which enhance polarizability. However, the conductivity decreased with increasing Fe_3O_4 concentration, as the formation of Fe^{3+} cross-linking bonds with silica tetrahedra increases glass rigidity and reduces ion mobility. Comparatively, ZrO_2-modified glasses exhibited a greater ability to reduce network rigidity and increase NBOs content (Figure 3), thereby enhancing ion mobility and electrical conductivity.

The results of the electrical study give insights on the impact of oxide insertion on the charge storage capabilities of bioglass. A higher dielectric constant enables greater polarization and thus increased charge storage. The insertion of ZrO_2 and Fe_3O_4 had a modest impact on the dielectric constant, with the 2 mol% ZrO_2 sample exhibiting the highest value. Moreover, conductivity proved to be a significant factor affecting charge trapping within the glass matrix. Bioglasses containing ZrO_2 demonstrated increased conductivity and enhanced ion mobility, which supported more efficient charge trapping. This indicates that the charge storage capability of these samples relies not only on their polarizability (as indicated by the dielectric constant) but also on the effectiveness of charge migration and trapping mechanisms within the glass structure.

3.3 Cytotoxicity

To assess the biocompatibility of the prepared bioglasses for potential biomedical applications, the viability of Saos-2 cells was evaluated after exposure to bioglass extracts. A resazurin assay was used to determine cell viability. As shown in Figure 8, the cytotoxicity of BG was significantly influenced by the type of metal oxide inserted into the bioglass network and the concentration of the extract. Non-passivated bioglass extracts containing ZrO_2, which were not preconditioned with McCoy's culture medium, exhibited significant cytotoxicity, reducing cell viability to less than 10% at a 100% extract concentration. In contrast, BG extracts with high Fe_3O_4 concentration demonstrated improved cell viability, even at a 100% extract concentration. While cytotoxic effects were still observed at higher concentrations, the findings suggest that Fe_3O_4 has a less pronounced cytotoxic effect than ZrO_2. All the bioglasses, except the 45S5 bioglass, demonstrated cell viability above 70% at a concentration of 25%, indicating their non-toxic effect on Saos-2 cells. This suggests that the insertion of ZrO_2, and Fe_3O_4 into BG can enhance the material's biocompatibility. These results are consistent with previous research (Mondal et al., 2013; Moghanian et al., 2020; Ezealigo et al., 2021). As illustrated in Figure 8, the passivation process effectively mitigated the cytotoxicity of the extracts. The cytotoxicity of bioglass is related to an increase in local pH resulting from ion-exchange reactions when the sample is exposed to a cell culture medium during the initial 24 h period (El-Rashidy et al., 2017). During this interaction, bioglass undergoes degradation of its

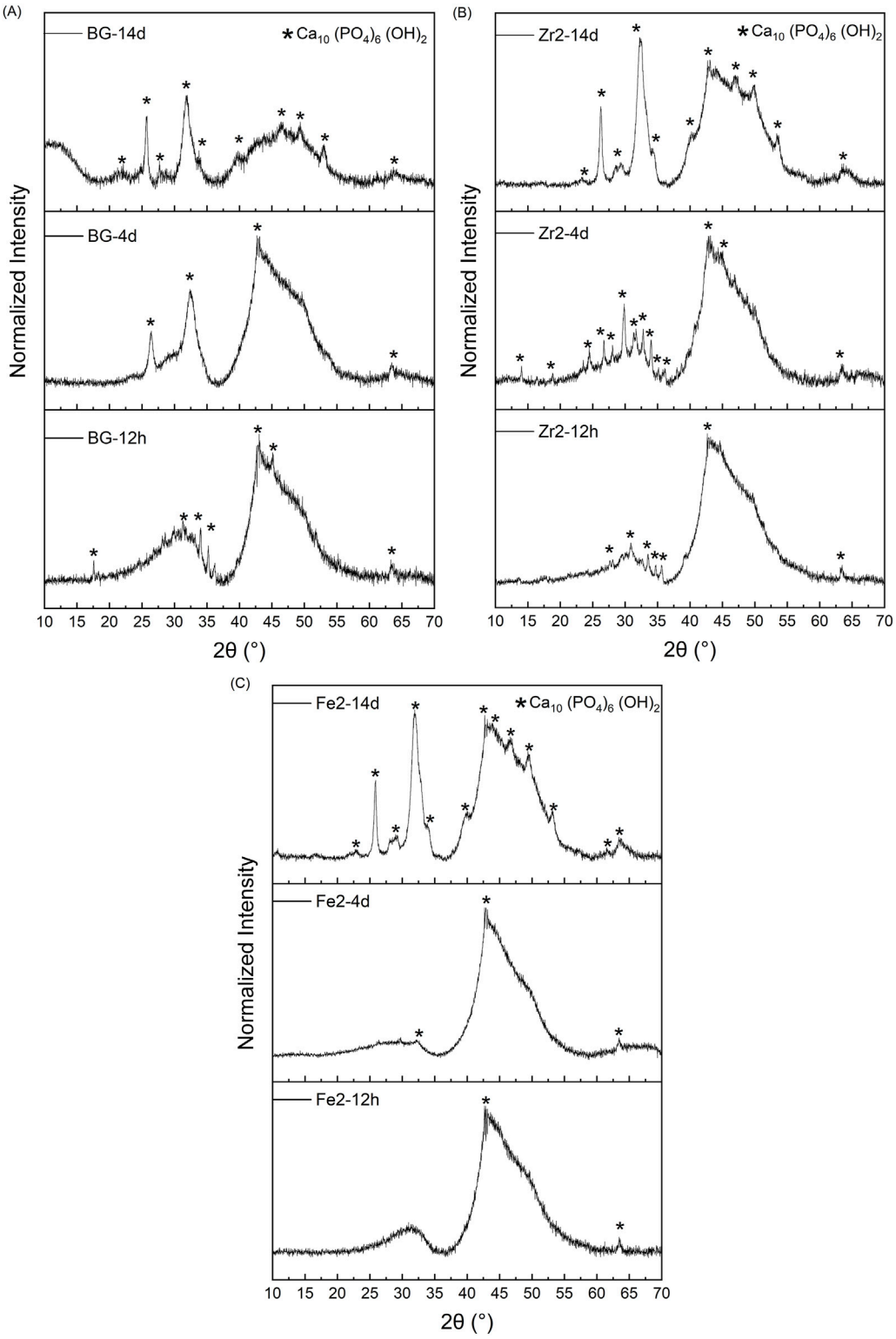

FIGURE 12
XRD patterns for **(A)** BG, **(B)** Zr2, and **(C)** Fe2 samples after SBF immersion for 12 h, 4 d, and 14 d.

Si-O-Si bonds, releasing soluble silica in the form of $Si(OH)_4$. This accelerates the dissolution rate and rises the pH of the surrounding environment, which can adversely impact cellular metabolism and function. However, it mitigates these alkalinization effects by establishing conditions that more closely resemble the *in vivo* environment, where living organisms actively regulate and maintain pH balance. The results obtained from the passivation process reveal that Fe_3O_4-containing bioglass exhibits excellent

biocompatibility. Specifically, bioglass containing 4 mol% Fe_3O_4 demonstrated high cell viability even at a 100% extract concentration. Furthermore, at a 50% extract concentration, all Fe_3O_4-modified BGs exhibited no cytotoxic effects on Saos-2 cells while for the ZrO_2-modified glasses, only the Zr4 does not show toxicity at this concentration. However, at 25% extract concentration all samples are no longer cytotoxic.

3.4 Antibacterial activity

Figure 9 illustrates the antibacterial properties of the samples, assessed using the agar disc diffusion method. All samples exhibited antibacterial activity, evidenced by the formation of inhibition zones surrounding the pellets. The average diameter of these zones exceeded 6 mm, the size of the pellets. Both the pH change toward alkalinity and the osmotic pressure generated by releasing ions like Na^+ and $Ca2^+$ into the surrounding media are major processes by which 45S5 BG inhibits bacterial growth (Hu et al., 2009; Drago et al., 2018). Additionally, incorporating oxides into the glass network can affect its antibacterial efficacy. An enhancement in the antibacterial properties of the bioglass was observed with the addition of ZrO_2. Among the samples, Zr2 exhibited the highest antimicrobial activity, with inhibition halos measuring 10.17 mm, 11.63 mm, and 9.63 mm against *E. coli*, *S. aureus*, and *S. mutans*, respectively. The improved antibacterial activity in the glass with 2 mol% ZrO_2 can be explained by the structural changes induced within the glass network. Through the fitting and deconvolution of Raman spectra (Figure 2), this sample showed the highest NBO content (Figure 3), suggesting a decrease in glass network connectivity. This reduced network connectivity due to the high concentration NBOs, facilitates the release of alkali metal ions (Na^+, and Ca^{2+}), leading to an increase in local pH, which promotes bacterial death. At higher ZrO_2 concentrations, the antibacterial activity decreased, which can be attributed to the formation of crystalline phases that strengthen the glass network, as confirmed by XRD analysis (Figure 1A). The addition of Fe_3O_4 to the base material resulted in a notable decrease in antibacterial effectiveness. This reduction in antimicrobial activity can be explained by the presence of iron, which polymerizes the glass structure by forming new cross-links with silica tetrahedra, consequently hindering its dissolution rate. The sample containing 2 mol% Fe_3O_4 demonstrated the highest antibacterial activity, with average inhibition halo diameters of 8.61 mm, 8.44 mm, and 9.01 mm against *E. coli*, *S. aureus*, and *S. mutans*, respectively.

3.5 Bioactivity evaluation

Figures 10A–C illustrate the changes in the atomic percentages of Si, Na, and the Ca/P ratio, respectively, as a function of immersion time on the surfaces of various bioglass samples. A substantial reduction in Si and Na concentrations was observed on the sample surfaces during the initial period, followed by stabilization in subsequent days. This behaviour is attributed to the dissolution of these elements into the surrounding medium, coupled with the formation of a Ca-P-rich layer. Indeed, when bioglass comes into contact with SBF, an immediate exchange occurs between the monovalent (Na^+) and divalent (Ca^{2+}) ions present in the glass and the H^+ ions in the fluid. The decrease in the amount of Na^+ on the glass surface is evident in Figure 10B. At the initial immersion time, for samples containing ZrO_2, this release is more pronounced, indicating higher glass reactivity. Compared to Fe_3O_4, the incorporation of ZrO_2 into the bioglass network facilitates network expansion and consequently increases the ionic dissolution rate. The formation of a silica gel layer on the glass surface enhances the diffusion of Ca^{2+} and PO_4^{3+} ions from the glass and the absorption of Ca and P ions from the solution, resulting in the formation of an amorphous calcium-phosphate layer. This series of reactions is illustrated in Figure 10A, C by the decrease in silicon and the decreasing Ca/P ratio, converging towards a value of 1.67, characteristic of hydroxyapatite (Beaufils et al., 2019; Boukha et al., 2019).

SEM micrographs of the surface of different bioglass samples after 0, 1, 4, and 14 d of immersion in SBF are shown in Figure 11. The formation of an apatitic layer on the surface was confirmed through SEM, revealing spherical particles with cauliflower-like morphologies, indicative of the bioactivity of the BGs. As immersion time increased, these apatite particles aggregated and became denser, eventually covering the entire surface after 14 d. These observations provide strong evidence of the osteoconductive potential of the prepared samples, demonstrating their ability to promote bone growth and regeneration. From Figure 11, it can be observed that the size and amount of spherical apatite particles formed on the bioglass surface, particularly during the initial days of SBF immersion, vary depending on the type and concentration of oxides inserted into the glass network. This variation in bioactivity is influenced by the structural changes induced by oxide insertion. Specifically, the presence of a depolymerized glass network facilitates ion exchange between the bioglass and SBF upon immersion, thereby enhancing bioactivity. The bioglass containing 2 mol% ZrO_2 exhibited a higher NBO content (Figure 3) which increased the mobility and release of network modifier ions (Na^+ and Ca^{2+}). This led to a rise in the glass dissolution rate during SBF immersion. Consequently, the sample containing 2 mol% ZrO_2 exhibited larger apatite particles during the initial days of SBF immersion, indicating enhanced bioactivity. However, when the ZrO_2 content exceeded 2 mol%, smaller apatite particles were observed during the early stages of immersion. This is likely due to the formation of crystalline phases, as confirmed by the XRD analysis, which increased glass rigidity and consequently reduced the dissolution rate and bioactivity. In contrast, bioglasses containing Fe_3O_4 demonstrated lower bioactivity compared to those with ZrO_2 and the 45S5 BG during the initial days of SBF immersion. This is evident in the SEM images, which show smaller apatite particles. This reduced bioactivity may be attributed to the stronger connectivity of the glass network, which limits ion release and consequently diminishes bioactivity.

Figures 12A–C show the XRD patterns of the 45S5 BG, Zr2, and Fe2 samples, respectively, after immersion in SBF for 12 h, 4 d, and 14 d to evaluate whether the Ca-P layer formed on the surface is amorphous or crystalline. Prior to SBF immersion, the XRD patterns (Figure 1A) displayed no distinct diffraction peaks, only a broad amorphous hump. After 12 h of immersion in SBF, a crystalline phase began to form, with a diffraction peak corresponding to hydroxyapatite, $Ca_{10}(PO_4)_6(OH)_2$ (ICCD No. 00-001–1,008) (Miola et al., 2015). As immersion time progressed, the crystallinity of the samples increased due to the growth of the hydroxyapatite layer on the surface. During the initial stages of immersion, 45S5 BG and Zr2 exhibited higher crystallinity compared to the Fe2 sample, indicating greater bioactivity. However, with prolonged immersion, the hydroxyapatite layer on the Fe2 sample became comparable to that of the other samples. This

suggests that while Fe initially reduces the bioactivity of the bioglass, it does not impede the long-term formation of hydroxyapatite. These findings are consistent with SEM-EDS results, confirming the bioactivity of the bioglasses.

4 Conclusion

In this work, a detailed investigation into the structural, electrical, and biological properties of bioactive glasses modified with ZrO_2, and Fe_3O_4 was conducted to evaluate their potential application as implant coatings. Our findings suggest that the introduction of these oxides led to changes in the glass network structure and connectivity. For the bioglass modified with ZrO_2, structural changes were identified through XRD analysis, with a high ZrO_2 content sample showing the emergence of crystalline phase. In the case of glasses modified with Fe_3O_4, Raman analysis detected the appearance of new vibrational modes associated with Fe-related structural units. The insertion of these oxides and the resulting structural changes significantly affected the bioglass connectivity, which in turn influenced its electrical and biological properties. Compared to Fe_3O_4, the insertion of the ZrO_2 into the bioglass network enhanced the conductivity and ion mobility. This improvement is attributed to the variation in the amount of non-bridging oxygen ions (NBOs), which was higher in glasses containing ZrO_2. These structural changes also influenced the antibacterial activity and bioactivity of the bioglasses. The samples modified with ZrO_2 demonstrated superior antibacterial activity and bioactivity compared to the base bioglass and the bioglass modified with Fe_3O_4. In contrast, the incorporation of Fe_3O_4 resulted in a reduction in both bioactivity and antibacterial activity. This decrease can be attributed to the effect of iron, which increases the rigidity of the glass network, thereby limiting ion release and reducing its bioactive and antibacterial performance. Among all the samples, the bioglass with 2mol% ZrO_2 showed the best antibacterial and bioactivity, suggesting that it is the most suitable for implant coating. The enhanced bioactivity observed in these glasses, particularly in the bioglass with 2 mol% ZrO_2, indicates their potential to promote osseointegration by facilitating the rapid formation of an apatite layer. This layer is critical for bonding implants to bone tissue and improving implant stability. Enhanced stability can reduce micromovements, thereby lowering the risk of bacterial infection. Furthermore, the superior antibacterial properties of these glasses suggest they could play a significant role in minimizing implant-associated infections, which remain a major challenge in clinical implantology. Moving forward, further studies focusing on *in vivo* testing are essential to validate the long-term stability and performance of these materials under physiological conditions. Such investigations are necessary to translate these findings into clinical practice and address existing challenges in implantology.

Data availability statement

The raw data supporting the conclusions of this article will be made available by the authors, without undue reservation.

Author contributions

IH: Data curation, Investigation, Methodology, Software, Writing–original draft. MG: Conceptualization, Funding acquisition, Project administration, Resources, Supervision, Validation, Visualization, Writing–review and editing. SG: Data curation, Formal Analysis, Investigation, Methodology, Writing–review and editing. JR: Data curation, Investigation, Methodology, Writing–review and editing. SJ: Data curation, Formal Analysis, Investigation, Methodology, Writing–review and editing. AP: Data curation, Formal Analysis, Investigation, Methodology, Writing–review and editing. JS: Conceptualization, Formal Analysis, Supervision, Validation, Visualization, Writing–review and editing. IS: Conceptualization, Formal Analysis, Investigation, Methodology, Supervision, Validation, Visualization, Writing–review and editing. JB: Conceptualization, Resources, Supervision, Validation, Visualization, Writing–review and editing.

Funding

The author(s) declare that financial support was received for the research, authorship, and/or publication of this article. This research was funded by FEDER funds through the COMPETE 2020 Program and National Funds through FCT—Portuguese Foundation for Science and Technology under the project LISBOA-01-0247-FEDER-039985/POCI-01-0247-FEDER-039985, LA/P/0037/2020, UIDP/50025/2020, and UIDB/50025/2020 of the Associate Laboratory Institute of Nanostructures, Nanomodelling and Nanofabrication—i3N, UIDP/04378/2020 and UIDB/04378/2020 of the Research Unit on Applied Molecular Biosciences—UCIBIO, and LA/P/0140/2020 of the Associate Laboratory Institute for Health and Bioeconomy—i4HB. S.R. Gavinho and A. Sofia Pádua acknowledge FCT—Portuguese Foundation for Science and Technology for the PhD grant (SFRH/BD/148233/2019 and UI/DB/151287/2021, respectively). S.K. Jakka acknowledges FCT—Fundaçao para a Ciência e a Tecnologia, Portugal, I.P., in the scope of the framework contract foreseen in the numbers 4, 5, and 6 of article 23 of the Decree Law 57/2016 of 29 August, changed by Law 57/2017 of 19 July.

Conflict of interest

The authors declare that the research was conducted in the absence of any commercial or financial relationships that could be construed as a potential conflict of interest.

The author(s) declared that they were an editorial board member of Frontiers, at the time of submission. This had no impact on the peer review process and the final decision.

Generative AI statement

The author(s) declare that no Generative AI was used in the creation of this manuscript.

Publisher's note

References

Abraham, C. M. (2014). A brief historical perspective on dental implants, their surface coatings and treatments. *Open Dent. J.* 8, 50–55. doi:10.2174/1874210601408010050

Addy, L. D. (2024). An introduction to dental implants. *Br. Dent. J.* 236, 753–757. doi:10.1038/s41415-024-7430-8

Aghili, F., Hoomehr, B., Saidi, R., and Raeissi, K. (2022). Synthesis and electrophoretic deposition of zinc oxide and zinc oxide-bioactive glass composite nanoparticles on AZ31 Mg Alloy for biomedical applications. *Ceram. Int.* 48, 34013–34024. doi:10.1016/j.ceramint.2022.08.001

Aguiar, H., Serra, J., González, P., and León, B. (2009). Structural study of sol–gel silicate glasses by IR and Raman spectroscopies. *J. Non-Crystalline Solids* 355, 475–480. doi:10.1016/j.jnoncrysol.2009.01.010

Aguiar, H., Solla, E. L., Serra, J., González, P., León, B., Almeida, N., et al. (2008). Orthophosphate nanostructures in SiO2–P2O5–CaO–Na2O–MgO bioactive glasses. *J. Non-Crystalline Solids* 354, 4075–4080. doi:10.1016/j.jnoncrysol.2008.05.031

Allan, I., Newman, H., and Wilson, M. (2001). Antibacterial activity of particulate Bioglass® against supra- and subgingival bacteria. *Biomaterials* 22, 1683–1687. doi:10.1016/S0142-9612(00)00330-6

Allan, I., Wilson, M., and Newman, H. (2002). Particulate Bioglass® reduces the viability of bacterial biofilms formed on its surface in an *in vitro* model. *Clin. Oral Implants Res.* 13, 53–58. doi:10.1034/j.1600-0501.2002.130106.x

Araujo, M. S., Silva, A. C., Bartolomé, J. F., and Mello-Castanho, S. (2020). Structural and thermal behavior of 45S5 Bioglass®-based compositions containing alumina and strontium. *J. Am. Ceram. Soc.* 103, 3620–3630. doi:10.1111/jace.17061

Ashok, J., Purnachand, N., Suresh Kumar, J., Srinivasa Reddy, M., Suresh, B., Graça, M. P. F., et al. (2017). Studies on dielectric dispersion, relaxation kinetics and a.c. conductivity of Na2OCuOSiO2 glasses mixed with Bi2O3-Influence of redox behavior of copper ions. *J. Alloys Compd.* 696, 1260–1268. doi:10.1016/j.jallcom.2016.12.080

Baert, K., Meulebroeck, W., Wouters, H., Cosyns, P., Nys, K., Thienpont, H., et al. (2011). Using Raman spectroscopy as a tool for the detection of iron in glass. *J. Raman Spectrosc.* 42, 1789–1795. doi:10.1002/jrs.2935

Barsoukov, E., and Macdonald, J. R. (2018). Impedance spectroscopy: theory, experiment, and applications. *John Wiley and Sons*. doi:10.1002/9781119381860

Beaufils, S., Rouillon, T., Millet, P., Le Bideau, J., Weiss, P., Chopart, J.-P., et al. (2019). Synthesis of calcium-deficient hydroxyapatite nanowires and nanotubes performed by template-assisted electrodeposition. *Mater. Sci. Eng. C* 98, 333–346. doi:10.1016/j.msec.2018.12.071

Begum, S., Johnson, W. E., Worthington, T., and Martin, R. A. (2016). The influence of pH and fluid dynamics on the antibacterial efficacy of 45S5 Bioglass. *Biomed. Mater.* 11, 015006. doi:10.1088/1748-6041/11/1/015006

Behera, S. S., Patra, J. K., Pramanik, K., Panda, N., and Thatoi, H. (2012). Characterization and evaluation of antibacterial activities of chemically synthesized iron oxide nanoparticles. Available at: http://repository.embuni.ac.ke/handle/123456789/1815 (Accessed June 12, 2024).

Bhowmick, A., Pramanik, N., Jana, P., Mitra, T., Gnanamani, A., Das, M., et al. (2017). Development of bone-like zirconium oxide nanoceramic modified chitosan based porous nanocomposites for biomedical application. *Int. J. Biol. Macromol.* 95, 348–356. doi:10.1016/j.ijbiomac.2016.11.052

Boccaccini, A. R., Chen, Q., Lefebvre, L., Gremillard, L., and Chevalier, J. (2007). Sintering, crystallisation and biodegradation behaviour of Bioglass®-derived glass–ceramics. *Faraday Discuss.* 136, 27–44. doi:10.1039/b616539g

Bose, S., Banerjee, D., Robertson, S., and Vahabzadeh, S. (2018). Enhanced *in vivo* bone and blood vessel formation by iron oxide and silica doped 3D printed tricalcium phosphate scaffolds. *Ann. Biomed. Eng.* 46, 1241–1253. doi:10.1007/s10439-018-2040-8

Boukha, Z., Yeste, M. P., Cauqui, M. Á., and González-Velasco, J. R. (2019). Influence of Ca/P ratio on the catalytic performance of Ni/hydroxyapatite samples in dry reforming of methane. *Appl. Catal. A General* 580, 34–45. doi:10.1016/j.apcata.2019.04.034

Cacciotti, I. (2017). Bivalent cationic ions doped bioactive glasses: the influence of magnesium, zinc, strontium and copper on the physical and biological properties. *J. Mater Sci.* 52, 8812–8831. doi:10.1007/s10853-017-1010-0

Chamritski, I., and Burns, G. (2005). Infrared- and Raman-active phonons of magnetite, maghemite, and hematite: a computer simulation and spectroscopic study. *J. Phys. Chem. B* 109, 4965–4968. doi:10.1021/jp048748h

Civantos, A., Martínez-Campos, E., Ramos, V., Elvira, C., Gallardo, A., and Abarrategi, A. (2017). Titanium coatings and surface modifications: toward clinically useful bioactive implants. *ACS Biomater. Sci. Eng.* 3, 1245–1261. doi:10.1021/acsbiomaterials.6b00604

Cociuban, C. L. M., Maghiar, T. T., Olariu, I., Vasca, E. M., Berari, A. R., Pasca, C., et al. (2024). Clinical-statistical study on oral rehabilitation methods using dental implants. *Med. Pharm. Rep.* 97, 398–404. doi:10.15386/mpr-2772

Davidson, D. J., Spratt, D., and Liddle, A. D. (2019). Implant materials and prosthetic joint infection: the battle with the biofilm. *EFORT open Rev.* 4, 633–639. doi:10.1302/2058-5241.4.180095

de Souza Balbinot, G., Leitune, V. C. B., Ponzoni, D., and Collares, F. M. (2019). Bone healing with niobium-containing bioactive glass composition in rat femur model: a micro-CT study. *Dent. Mater.* 35, 1490–1497. doi:10.1016/j.dental.2019.07.012

Di Muro, A., Métrich, N., Mercier, M., Giordano, D., Massare, D., and Montagnac, G. (2009). Micro-Raman determination of iron redox state in dry natural glasses: application to peralkaline rhyolites and basalts. *Chem. Geol.* 259, 78–88. doi:10.1016/j.chemgeo.2008.08.013

Drago, L., Toscano, M., and Bottagisio, M. (2018). Recent evidence on bioactive glass antimicrobial and antibiofilm activity: a mini-review. *Materials* 11, 326. doi:10.3390/ma11020326

Dziadek, M., Zagrajczuk, B., Jelen, P., Olejniczak, Z., and Cholewa-Kowalska, K. (2016). Structural variations of bioactive glasses obtained by different synthesis routes. *Ceram. Int.* 42, 14700–14709. doi:10.1016/j.ceramint.2016.06.095

El-Mallawany, R. A. (2014). *Tellurite glasses handbook: physical properties and data*. United States: CRC Press. doi:10.1201/b11295

El-Rashidy, A. A., Roether, J. A., Harhaus, L., Kneser, U., and Boccaccini, A. R. (2017). Regenerating bone with bioactive glass scaffolds: a review of *in vivo* studies in bone defect models. *Acta biomater.* 62, 1–28. doi:10.1016/j.actbio.2017.08.030

Ezealigo, U. S., Ezealigo, B. N., Aisida, S. O., and Ezema, F. I. (2021). Iron oxide nanoparticles in biological systems: antibacterial and toxicology perspective. *JCIS Open* 4, 100027. doi:10.1016/j.jciso.2021.100027

Fathima, J. B., Pugazhendhi, A., and Venis, R. (2017). Synthesis and characterization of ZrO2 nanoparticles-antimicrobial activity and their prospective role in dental care. *Microb. Pathog.* 110, 245–251. doi:10.1016/j.micpath.2017.06.039

Gavinho, S. R., Hammami, I., Jakka, S. K., Teixeira, S. S., Silva, J. C., Borges, J. P., et al. (2024). Influence of the addition of zinc, strontium, or magnesium oxides to the bioglass 45S5 network on electrical behavior. *Materials* 17, 499. doi:10.3390/ma17020499

Gbejuade, H. O., Lovering, A. M., and Webb, J. C. (2015). The role of microbial biofilms in prosthetic joint infections. *Acta Orthop.* 86, 147–158. doi:10.3109/17453674.2014.966290

Goo, H. W., Kim, I.-J., and Shin, S.-Y. (2018). Comparative study of new bone formation capability of zirconia bone graft material in rabbit calvarial. *J. Adv. Prosthodont.* 19, 167–176. doi:10.4047/jap.2018.10.3.167

Graça, M. P. F., Rudnitskaya, A., Faria, F. A. C., Evtuguin, D. V., Gomes, M. T. S. R., Oliveira, J. A. B. P., et al. (2012). Electrochemical impedance study of the lignin-derived conducting polymer. *Electrochimica Acta* 76, 69–76. doi:10.1016/j.electacta.2012.04.155

Hammami, I., Graça, M. P. F., Gavinho, S. R., Jakka, S. K., Borges, J. P., Silva, J. C., et al. (2024). Exploring the impact of copper oxide substitution on structure, morphology, bioactivity, and electrical properties of 45S5 Bioglass®. *Biomimetics* 9, 213. doi:10.3390/biomimetics9040213

Hammami, I., Sales, A. M. J., Benhamou, K., Arous, M., Costa, L. C., da Cruz, J. A., et al. (2022). Dielectric response and molecular dynamics of nanocomposites based on TEMPO-oxidized cellulose nanofibrils and polyvinyl acetate. *Therm. Sci. Eng. Prog.* 34, 101428. doi:10.1016/j.tsep.2022.101428

Hempel, U., Hefti, T., Kalbacova, M., Wolf-Brandstetter, C., Dieter, P., and Schlottig, F. (2010). Response of osteoblast-like SAOS-2 cells to zirconia ceramics with different surface topographies. *Clin. oral implants Res.* 21, 174–181. doi:10.1111/j.1600-0501.2009.01797.x

Hench, L. L. (2006). The story of Bioglass®. *J. Mater. Sci. Mater. Med.* 17, 967–978. doi:10.1007/s10856-006-0432-z

Hench, L. L. (2013). *An introduction to bioceramics*. Second Edition, 1–600. doi:10.1142/P884/SUPPL_FILE/P884_CHAP03.PDF

Hench, L. L., and Paschall, H. A. (1973). Direct chemical bond of bioactive glass-ceramic materials to bone and muscle. *J. Biomed. Mater. Res.* 7, 25–42. doi:10.1002/jbm.820070304

Hench, L. L., Splinter, R. J., Allen, W. C., and Greenlee, T. K. (1971). Bonding mechanisms at the interface of ceramic prosthetic materials. *J. Biomed. Mater. Res.* 5, 117–141. doi:10.1002/jbm.820050611

Hu, S., Chang, J., Liu, M., and Ning, C. (2009). Study on antibacterial effect of 45S5 Bioglass®. *J. Mater. Sci. Mater. Med.* 20, 281–286. doi:10.1007/s10856-008-3564-5

Ibrahim, N. F., Mohamad, H., and Noor, S. N. F. M. (2017). Characterization on melt-derived bioactive glass powder from SiO2-CaO-Na2O-P2O5 system. *J. Non-Crystalline Solids* 462, 23–31. doi:10.1016/j.jnoncrysol.2017.01.040

Ibrahim, N. F., Mohamad, H., Noor, S. N. F. M., and Ahmad, N. (2018). Melt-derived bioactive glass based on SiO2-CaO-Na2O-P2O5 system fabricated at lower melting temperature. *J. Alloys Compd.* 732, 603–612. doi:10.1016/j.jallcom.2017.10.235

Jangra, S. L., Stalin, K., Dilbaghi, N., Kumar, S., Tawale, J., Singh, S. P., et al. (2012). Antimicrobial activity of zirconia (ZrO2) nanoparticles and zirconium complexes. *J. Nanosci. Nanotechnol.* 12, 7105–7112. doi:10.1166/jnn.2012.6574

Kang, T.-Y., Seo, J.-Y., Ryu, J.-H., Kim, K.-M., and Kwon, J.-S. (2021). Improvement of the mechanical and biological properties of bioactive glasses by the addition of zirconium oxide (ZrO2) as a synthetic bone graft substitute. *J. Biomed. Mater. Res. Part A* 109, 1196–1208. doi:10.1002/jbm.a.37113

Kawamura, J., Yoshikado, S., Sakuma, T., Michihiro, Y., Aniya, M., and Ito, Y. (2007). Superionic conductor physics-proceedings of the 1st international meeting on superionic conductor physics (idmsicp). *World Sci.* Available at: https://books.google.com/books?hl=en&lr=&id=3GbICgAAQBAJ&oi=fnd&pg=PR11&dq=Superionic+Conductor+Physics-Proceedings+of+the+1st+International+Meeting+On+Superionic+Conductor+Physics&ots=U2Q1fT-Uia&sig=FwvW7QeDcgEkBjWUP0UGhCdNejE (Accessed November 15, 2024).

Keshri, S. R., Ganisetti, S., Kumar, R., Gaddam, A., Illath, K., Ajithkumar, T. G., et al. (2021). Ionic conductivity of Na3Al2P3O12 glass electrolytes—role of charge compensators. *Inorg. Chem.* 60, 12893–12905. doi:10.1021/acs.inorgchem.1c01280

Kobayashi, T., Nakamura, S., and Yamashita, K. (2001). Enhanced osteobonding by negative surface charges of electrically polarized hydroxyapatite. *J. Biomed. Mater. Res.* 57, 477–484. doi:10.1002/1097-4636(20011215)57:4<477::AID-JBM1193>3.0.CO;2-5

Kumar, P., Kumar, V., Kumar, R., Kumar, R., and Pruncu, C. I. (2020). Fabrication and characterization of ZrO2 incorporated SiO2–CaO–P2O5 bioactive glass scaffolds. *J. Mech. Behav. Biomed. Mater.* 109, 103854. doi:10.1016/j.jmbbm.2020.103854

Li, Y.-S., Church, J. S., and Woodhead, A. L. (2012). Infrared and Raman spectroscopic studies on iron oxide magnetic nano-particles and their surface modifications. *J. Magnetism Magnetic Mater.* 324, 1543–1550. doi:10.1016/j.jmmm.2011.11.065

Long, T., Guo, Y.-P., Tang, S., Guo, Y.-J., and Zhu, Z.-A. (2014). Emulsion fabrication of magnetic mesoporous carbonated hydroxyapatite microspheres for treatment of bone infection. *RSC Adv.* 4, 11816–11825. doi:10.1039/c3ra45896b

Lopes, J. H., Magalhães, A., Mazali, I. O., and Bertran, C. A. (2014). Effect of niobium oxide on the structure and properties of melt-derived bioactive glasses. *J. Am. Ceram. Soc.* 97, 3843–3852. doi:10.1111/jace.13222

Macdonald, Jr. (1987). "Emphasizing solid materials and systems," in *Impedance spectroscopy* (New York, NY, USA: John Wiley and Sons Inc.).

Malavasi, G., Salvatori, R., Zambon, A., Lusvardi, G., Rigamonti, L., Chiarini, L., et al. (2019). Cytocompatibility of potential bioactive cerium-doped glasses based on 45S5. *Materials* 12, 594. doi:10.3390/ma12040594

Metwally, S., and Stachewicz, U. (2019). Surface potential and charges impact on cell responses on biomaterials interfaces for medical applications. *Mater. Sci. Eng. C* 104, 109883. doi:10.1016/j.msec.2019.109883

Miola, M., Verné, E., Ciraldo, F. E., Cordero-Arias, L., and Boccaccini, A. R. (2015). Electrophoretic deposition of chitosan/45S5 bioactive glass composite coatings doped with Zn and Sr. *Front. Bioeng. Biotechnol.* 3, 159. doi:10.3389/fbioe.2015.00159

Moghanian, A., Zohourfazeli, M., and Tajer, M. H. M. (2020). The effect of zirconium content on *in vitro* bioactivity, biological behavior and antibacterial activity of sol-gel derived 58S bioactive glass. *J. Non-Crystalline Solids* 546, 120262. doi:10.1016/j.jnoncrysol.2020.120262

Mondal, D., So-Ra, S., and Lee, B. T. (2013). Fabrication and characterization of ZrO2–CaO–P2O5–Na2O–SiO2 bioactive glass ceramics. *J. Mater Sci.* 48, 1863–1872. doi:10.1007/s10853-012-6956-3

Nayak, M. T., and Desa, J. A. E. (2018). Roles of iron and lithium in silicate glasses by Raman spectroscopy. *J. Raman Spectrosc.* 49, 1507–1513. doi:10.1002/jrs.5397

Obata, A., Nakamura, S., Moriyoshi, Y., and Yamashita, K. (2003). Electrical polarization of bioactive glass and assessment of their *in vitro* apatite deposition. *J. Biomed. Mater. Res. Part A* 67, 413–420. doi:10.1002/jbm.a.10069

Obata, A., Nakamura, S., and Yamashita, K. (2004). Interpretation of electrical polarization and depolarization mechanisms of bioactive glasses in relation to ionic migration. *Biomaterials* 25, 5163–5169. doi:10.1016/j.biomaterials.2003.12.028

Ohgaki, M., Kizuki, T., Katsura, M., and Yamashita, K. (2001). Manipulation of selective cell adhesion and growth by surface charges of electrically polarized hydroxyapatite. *J. Biomed. Mater. Res.* 57, 366–373. doi:10.1002/1097-4636(20011205)57:3<366::AID-JBM1179>3.0.CO;2-X

Pattnaik, S., Nethala, S., Tripathi, A., Saravanan, S., Moorthi, A., and Selvamurugan, N. (2011). Chitosan scaffolds containing silicon dioxide and zirconia nano particles for bone tissue engineering. *Int. J. Biol. Macromol.* 49, 1167–1172. doi:10.1016/j.ijbiomac.2011.09.016

Prezas, P. R., Melo, B. M. G., Costa, L. C., Valente, M. A., Lança, M. C., Ventura, J. M. G., et al. (2017). TSDC and impedance spectroscopy measurements on hydroxyapatite, β-tricalcium phosphate and hydroxyapatite/β-tricalcium phosphate biphasic bioceramics. *Appl. Surf. Sci.* 424, 28–38a. doi:10.1016/j.apsusc.2017.02.225

Rad Goudarzi, M., Bagherzadeh, M., Fazilati, M., Riahi, F., Salavati, H., and Shahrokh Esfahani, S. (2019). Evaluation of antibacterial property of hydroxyapatite and zirconium oxide-modificated magnetic nanoparticles against *Staphylococcus aureus* and *Escherichia coli*. *IET nanobiotechnol* 13, 449–455. doi:10.1049/iet-nbt.2018.5029

Sa, M., Nguyen, B. B., Moriarty, R. A., Kamalitdinov, T., Fisher, J. P., and Kim, J. Y. (2018). Fabrication and evaluation of 3D printed BCP scaffolds reinforced with ZrO_2 for bone tissue applications. *Biotech and Bioeng.* 115, 989–999. doi:10.1002/bit.26514

Silva, C. C., Valente, M. A., Graça, M. P. F., and Sombra, A. S. B. (2004). Preparation and optical characterization of hydroxyapatite and ceramic systems with titanium and zirconium formed by dry high-energy mechanical alloying. *Solid State Sci.* 6, 1365–1374. doi:10.1016/j.solidstatesciences.2004.07.009

Silva, C. C., Valente, M. A., Graça, M. P. F., and Sombra, A. S. B. (2005). The modulus formalism used in the dielectric analysis of hydroxyapatite and calcium phosphate with titanium formed by dry ball milling. *J. Non-Crystalline Solids* 351, 2945–2950. doi:10.1016/j.jnoncrysol.2005.04.082

Silva, R. C. S., Agrelli, A., Andrade, A. N., Mendes-Marques, C. L., Arruda, I. R. S., Santos, L. R. L., et al. (2022). Titanium dental implants: an overview of applied nanobiotechnology to improve biocompatibility and prevent infections. *Materials* 15, 3150. doi:10.3390/ma15093150

Theil, E. C., and Goss, D. J. (2009). Living with iron (and oxygen): questions and answers about iron homeostasis. *Chem. Rev.* 109, 4568–4579. doi:10.1021/cr900052g

Touati, D. (2000). Iron and oxidative stress in bacteria. *Archives Biochem. biophysics* 373, 1–6. doi:10.1006/abbi.1999.1518

Ullah, I., Zhang, W., Yang, L., Ullah, M. W., Atta, O. M., Khan, S., et al. (2020). Impact of structural features of Sr/Fe co-doped HAp on the osteoblast proliferation and osteogenic differentiation for its application as a bone substitute. *Mater. Sci. Eng. C* 110, 110633. doi:10.1016/j.msec.2020.110633

Wang, Z., Cooney, T. F., and Sharma, S. K. (1995). *In situ* structural investigation of iron-containing silicate liquids and glasses. *Geochimica Cosmochimica Acta* 59, 1571–1577. doi:10.1016/0016-7037(95)00063-6

Yamashita, K., Oikawa, N., and Umegaki, T. (1996). Acceleration and deceleration of bone-like crystal growth on ceramic hydroxyapatite by electric poling. *Chem. Mater.* 8, 2697–2700. doi:10.1021/cm9602858

Zhang, C., He, Y., Xu, Z., Shi, H., Di, H., Pan, Y., et al. (2016). Fabrication of Fe3O4@SiO2 nanocomposites to enhance anticorrosion performance of epoxy coatings. *undefined* 27, 740–747. doi:10.1002/PAT.3707

Zhang, Z., Zhang, N., Li, X., Li, G., Zhang, K., Jing, A., et al. (2022). Porous magnetic Fe3O4/bioactive glass–ceramic (CaO-SiO2-P2O5-MgO) scaffold with enhanced self-heating ability for hyperthermia treatment of bone tumor—an *in vitro* study. *J. Aust. Ceram. Soc.* 58, 1729–1745. doi:10.1007/s41779-022-00807-1

Zhou, T., Xu, Z., Sun, H., Beltrán, A. M., Nawaz, Q., Sui, B., et al. (2024). Unlocking the potential of iron-containing mesoporous bioactive glasses: orchestrating osteogenic differentiation in bone marrow mesenchymal stem cells and osteoblasts. *Colloids Surfaces A Physicochem. Eng. Aspects* 694, 134188. doi:10.1016/j.colsurfa.2024.134188

Zhu, W., Li, C., Yao, M., Wang, X., Wang, J., Zhang, W., et al. (2023). Advances in osseointegration of biomimetic mineralized collagen and inorganic metal elements of natural bone for bone repair. *Regen. Biomater.* 10, rbad030. doi:10.1093/rb/rbad030